Earth and Planetary Science Letters 531 (2020) 115967

Contents lists available at ScienceDirect

Earth and Planetary Science Letters

www.elsevier.com/locate/epsl

The role of metasomatic alteration on frictional properties of subduction thrusts: An example from a serpentinite body in the Franciscan Complex, California

Ken-ichi Hirauchi [a,*], Yuzuru Yamamoto [b], Sabine A.M. den Hartog [c], André R. Niemeijer [d]

[a] Department of Geosciences, Faculty of Science, Shizuoka University, 836 Ohya, Suruga-ku, Shizuoka 422-8529, Japan
[b] Department of Mathematical Science and Advanced Technology, Japan Agency for Marine-Earth Science and Technology, Showa-machi 3173-25, Kanazawa-ku, Yokohama 236-0001, Japan
[c] The Lyell Centre, Heriot-Watt University, Research Avenue South, Edinburgh, EH14 4AP, UK
[d] Department of Earth Sciences, Utrecht University, Budapestlaan 4, 3584 CD Utrecht, the Netherlands

ARTICLE INFO

Article history:
Received 31 January 2019
Received in revised form 26 October 2019
Accepted 8 November 2019
Available online 25 November 2019
Editor: J. Brodholt

Keywords:
Franciscan Complex
friction
interplate coupling
metasomatism
serpentinite

ABSTRACT

Fluid–rock interaction within accretionary prisms drastically changes the frictional strength and slip stability of the fault zone. In order to understand the effect of ultramafic components on the degree of interplate coupling, we present data on frictional properties of a reaction zone between serpentinite and argillite in a tectonic mélange of the Franciscan Complex, central California. Field and petrographic observations indicate that the argillite and serpentinite along the lithological boundary are metasomatized to tremolite and talc schists, respectively, forming a ductile shear zone. Simulated gouges made from fault and wall rock samples collected are sheared at effective normal stresses (σ_n^{eff}) of 60–180 MPa and temperatures (T) of 20–400 °C, using a hydrothermal ring shear machine. The serpentinite is frictionally strong (steady-state friction coefficient $\mu_{ss} = 0.5$–0.6), and exhibits both velocity-weakening and velocity-strengthening behavior. The μ_{ss} of the argillite and tremolite schist increases up to 0.7 and 0.6, respectively, with increasing σ_n^{eff} and T, while $(a - b)$ transitions from positive to negative with increasing T. At a given experimental condition, μ and $(a - b)$ values are lower and higher for the tremolite schist than for the argillite. In contrast, the talc schist exhibits very low friction ($\mu_{ss} = 0.1$–0.2) and velocity-strengthening behavior at all experimental conditions tested. Our results demonstrate that Si-metasomatism along the argillite–serpentinite contact results in reduced friction and stabilized slip, forming frictionally weak, velocity-strengthening regions in the megathrust zone.

1. Introduction

Most large earthquakes (with moment magnitude $M_w > 7$) occur on the thrust fault between subducting and overriding plates. The extent of the so-called seismogenic zone in subduction zones appears to be thermally controlled, with updip and downdip limits occurring at 100–150 °C and 350–450 °C, respectively (e.g., Oleskevich et al., 1999). The updip limit of seismicity is attributed to the dehydration reaction of smectite to form illite (Vrolijk, 1990) or lithification of underthrusting sediments (Moore et al., 2007; Trütner et al., 2015), while the downdip limit coincides with a transition from velocity-weakening to velocity-strengthening behavior of quartzo-feldspathic rocks or argillaceous sediments, induced by the thermal activation of viscous (plastic) processes in quartz (Blanpied et al., 1995; den Hartog et al., 2012a). Alternatively, if the intersection of the thrust fault with the overriding plate Moho is located at shallower depths than the 350 °C isotherm, stable frictional sliding or plastic flow of serpentine at the base of the hydrated forearc mantle wedge may inhibit the generation of subduction thrust earthquakes (Hirauchi et al., 2010; Takahashi et al., 2011).

Geodetic and seismological observations indicate that in the seismogenic zone, there are spatial and temporal variations in interplate coupling along both strike and dip directions (e.g., Suwa et al., 2006; Burgette et al., 2009; Uchida et al., 2009; Yoshioka and Matsuoka, 2013). The heterogeneity of interplate coupling may be explained by the presence of seamounts and other topographic reliefs on the subducting plate (Wang and Bilek, 2011), or by fluid content in a plate-boundary shear zone (Heise et al., 2017). On the other hand, the differences in interplate coupling are linked to those in fault slip behavior, including continuous aseismic sliding and episodic earthquake slip. As mineralogy is one of the factors

* Corresponding author.
E-mail address: hirauchi.kenichi@shizuoka.ac.jp (K.-i. Hirauchi).

https://doi.org/10.1016/j.epsl.2019.115967
0012-821X/

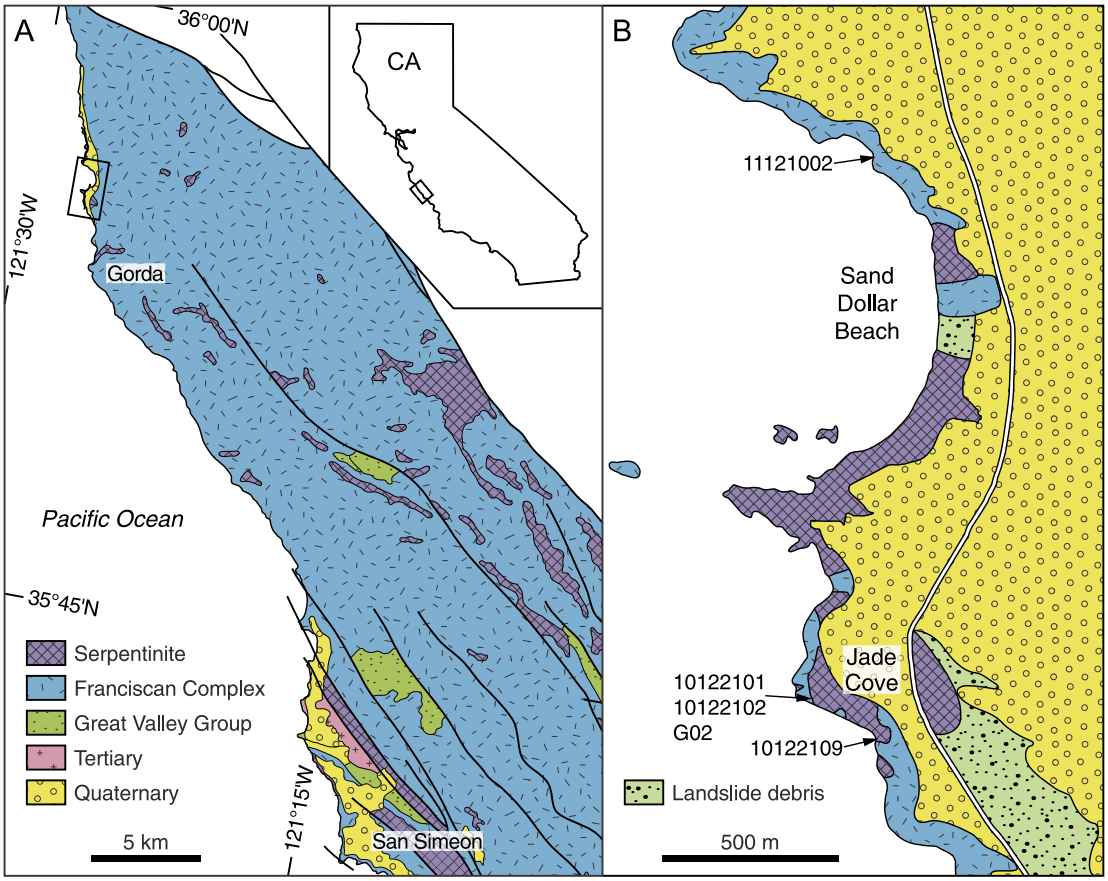

Fig. 1. (A) Geologic map of the western margin of central California, showing rock units, major faults, modified from Jennings (1958) and King et al. (2003). (B) Enlargement of the area shown in (A) (black rectangle), showing sample localities at Sand Dollar Beach and Jade Cove, Monterey County. All samples except for sample G02 were collected from outcrop. (For interpretation of the colors in the figure(s), the reader is referred to the web version of this article.)

that control the nucleation of slip instability, the composition of fault zone materials plays a key role in controlling the degree of interplate coupling. For instance, Ikari et al. (2013) suggested that at nonaccretionary margins, the type of sediment cover (i.e., carbonates or clays) on the subducting oceanic plate controls the loci of earthquake nucleation along the megathrust.

Aqueous fluids expelled from the subducting slab are predicted to be focused into a permeable plate boundary shear zone. Fluids act not only to reduce the effective normal stress (σ_n^{eff}) on the fault, but also to promote mass transfer of fluid-mobile elements (e.g., Bebout and Penniston-Dorland, 2016). The fluid-assisted mass transfer in accretionary prisms results in the formation of quartz and carbonate veins (Moore et al., 2007), providing a potential preferential site for earthquake nucleation (Chester and Higgs, 1992; Verberne et al., 2013). On the other hand, in places where disparate rock types (e.g., mafic vs. ultramafic lithologies) are in contact with one another, metasomatic alteration of both rocks occurs through diffusion across a chemical potential gradient, leading to the development of reaction zones consisting mainly of hydrous minerals (e.g., amphiboles, chlorites, serpentines and talc). Petrological and geochemical studies have provided information about element mobility due to mass transfer during metasomatic alteration of ultramafic blocks in subduction zone complexes (e.g., Bebout and Barton, 2002; Spandler et al., 2008). However, it remains unclear how metasomatic alteration changes deformation behavior of a shear zone localized along the lithological contacts in terms of seismicity.

The importance of talc metasomatism on fault zone properties has been documented in several field and experimental studies (Moore and Rymer, 2007; Escartín et al., 2008a; Collettini et al., 2009a,b; Holdsworth et al., 2011; Hirauchi et al., 2013; Moore and Lockner, 2011, 2013). In this study, we describe a talc-bearing, metasomatic reaction zone developed between serpentinite and argillite in a tectonic mélange of the Franciscan accretionary prism, Gorda, central California. The serpentinite represents a fragment of abyssal peridotite exposed along oceanic transform or detachment faults (Coleman, 2000; Hirauchi et al., 2008). The samples collected are utilized for hydrothermal frictional sliding experiments conducted over a wide range of pressure and temperature conditions ($\sigma_n^{eff} = 60$–180 MPa, $T = 20$–$400\,^{\circ}$C), in order to investigate the extent to which metasomatic alteration affects frictional strength and slip stability of subduction thrust faults at seismogenic depths. Based on field and experimental data, we discuss the influence of ultramafic components on the degree of interplate coupling.

2. Geologic setting and deformation features of an ancient subduction fault

At Gorda, several serpentinite bodies up to 500 m thick, striking NW–SE and moderately to steeply dipping to the NE, are well exposed on Sand Dollar Beach and Jade Cove along a length of 3 km, and are incorporated into the Late Cretaceous Franciscan accretionary complex (Fig. 1) (Ernst, 2011). The Franciscan Complex in the study area that is present in the Central Belt represents a tectonic mélange characterized by blocks of metagreywacke, greenstone, and metachert within an argillite matrix (e.g., Hall, 1991). Mineral assemblages of the metagraywacke include pumpellyite ± prehnite, metamorphosed at temperatures of $150 \pm 50\,^{\circ}$C and pressures of 2–3 kbar (Ernst, 1980), corresponding to P–T conditions

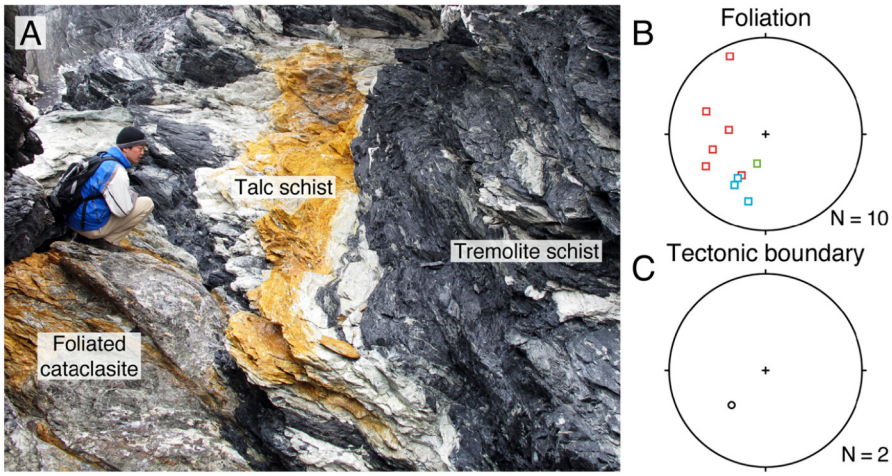

Fig. 2. Occurrence of a reaction zone between argillite and serpentinite within the Franciscan Complex at Jade Cove. (A) Outcrop photograph showing lenses and layers of talc schist embedded within tremolite schist. (B and C) Stereoplots illustrating poles to foliation (B) and lithological contacts between foliated cataclasite and tremolite schist (C). All plots are shown on lower hemisphere, equal area projections. Blue squares: foliated cataclasite, green square: talc schist, red squares: tremolite schist.

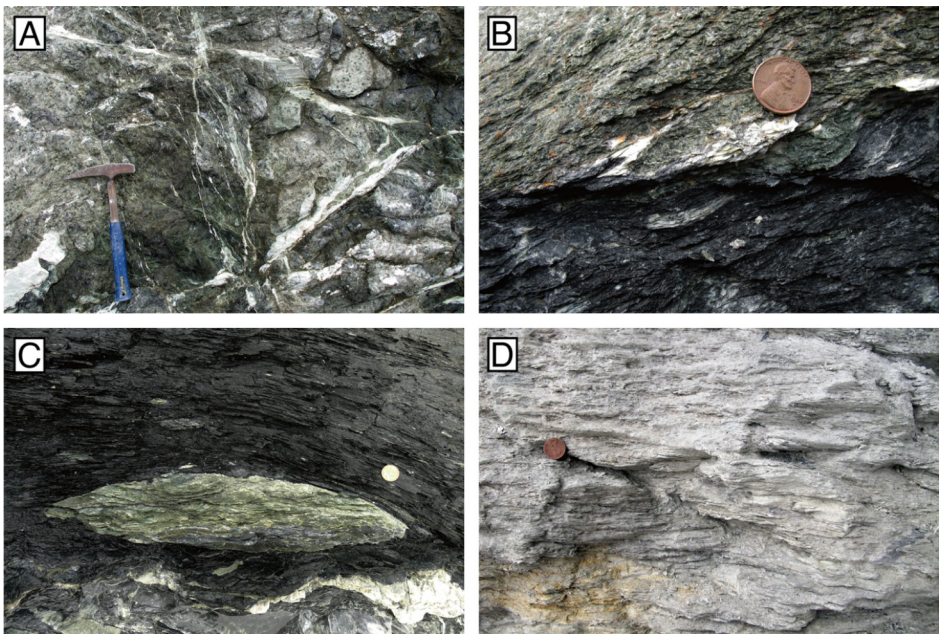

Fig. 3. Outcrop photographs showing metasomatic features at Jade Cove. (A) Blocky serpentinite crosscut by serpentine and talc veins. (B) Close up of a lithological boundary between foliated cataclasite and tremolite schist. The foliated cataclasite is accompanied with vein networks of talc. (C) Lenticular serpentinite (now altered to talc-rich assemblages) blocks embedded in tremolite schist. (D) Close up of talc schist in Fig. 2A.

for the upper part of the seismogenic zone in subduction zones (Oleskevich et al., 1999). The argillite matrix that displays a penetrative scaly fabric is composed mainly of clay minerals, such as illite/muscovite and chlorite, along with fragments of quartz, plagioclase, epidote, and calcite. The scaly cleavages are defined by preferentially oriented clay minerals and dark pressure-solution seams (Fig. 4A, B), suggesting that the main deformation mechanism is frictional sliding on phyllosilicate foliation, with accommodation by pressure solution of quartz grains (e.g., Niemeijer, 2018).

The serpentinite body along Sand Dollar Beach exhibits a block-in-matrix structure, consisting of a sheared chrysotile matrix that wraps around phacoids, in which multiple serpentinization events, including the lizardite/chrysotile–antigorite transition indicative of high-temperature ($T > 250$–$300\,^{\circ}$C) metamorphism (Evans, 2004; Schwartz et al., 2013), are recognized (King et al., 2003; Hirauchi and Yamaguchi, 2007; Hirauchi et al., 2008). The low-temperature, chrysotile-bearing deformation represents a retrograde episode, possibly related to the exhumation along the subduction boundary. Petrological and geochemical characteristics of relict primary minerals within the phacoids (spinel lherzolite) are typical of abyssal peridotites sampled at slow-spreading mid-ocean ridges (Hirauchi et al., 2008), representing 'Franciscan peridotite wedges' that are thought to be tectonically detached slabs of abyssal peridotite that had been exposed near the seafloor (Coleman, 2000). Thus, the serpentinite bodies in the study area are regarded as oceanic mantle rocks that were subducted from the trench to great depths, and then were exhumed in a subduction channel and ultimately underplated to the Franciscan accretionary complex.

At Jade Cove, there are several boundary faults (striking WNW–ESE and moderately dipping to the NE) that separate the serpentinite bodies from the Franciscan mélanges (Fig. 2) (King et al., 2003). The serpentinite body that shows a block-in-matrix structure is overprinted by anastomosing development of crack-seal veins of serpentine (antigorite or lizardite) and talc (Figs. 3A and 4C), the amount of which increases towards the boundary fault over a distance of ∼10–50 m. This observation suggests that in-

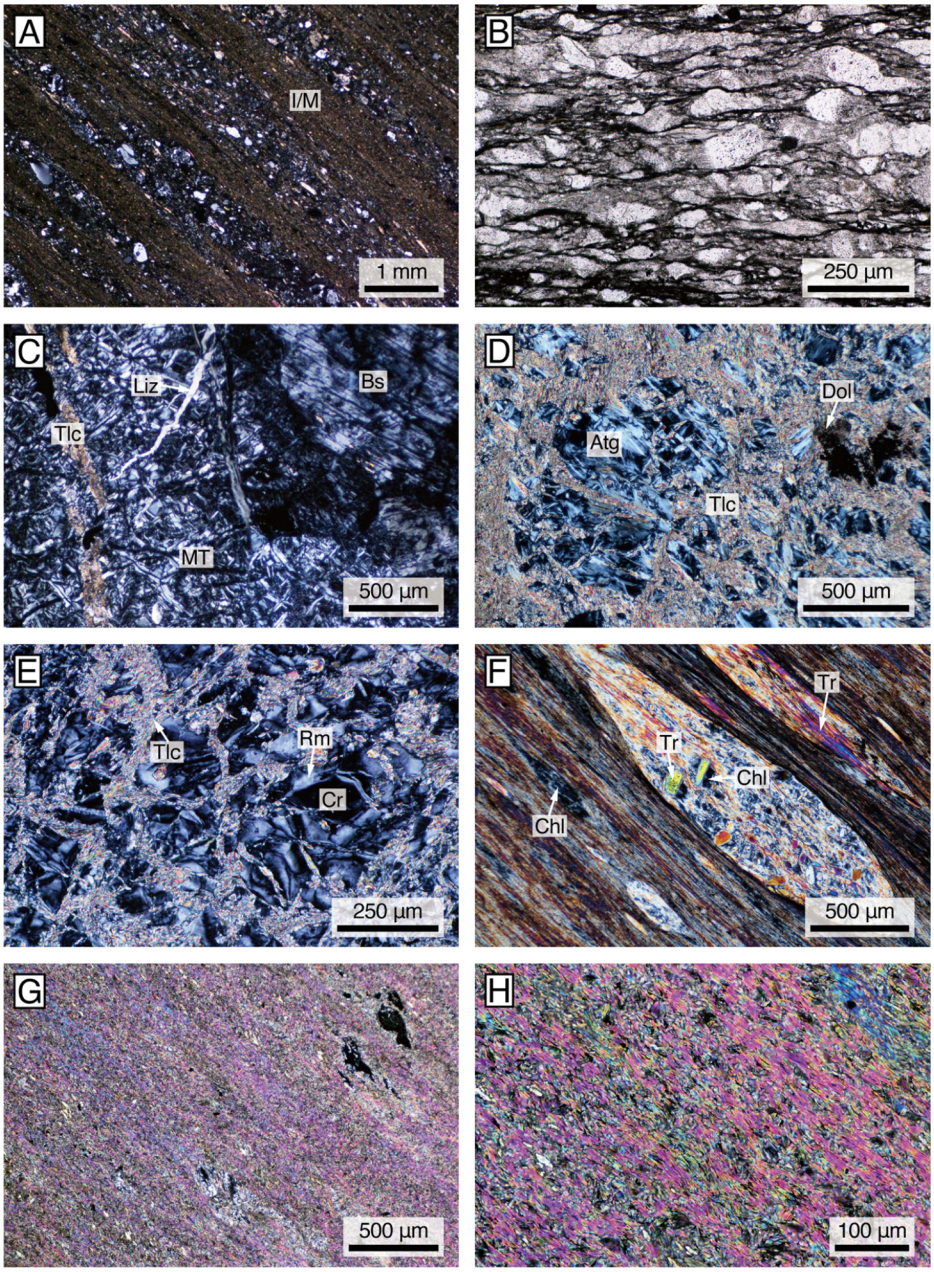

Fig. 4. Optical photomicrographs of metasomatic (talc and tremolite schists) and non-metasomatic (argillite and serpentinite) rock samples used for friction experiments. The photomicrographs were taken in plane-polarized light (B) and in cross-polarized light (A, C, D, E, F, G and H). (A and B) Argillite (sample no.: 11121002) with preferentially oriented illite/muscovite (I/M) aggregates (A) and dark pressure-solution seams and soluble minerals such as quartz and plagioclase (B). (C) Massive serpentinite (sample no.: 10122109) exhibiting mesh (hourglass) texture (MT) and bastite (Bs). Note crosscutting veins of lizardite (liz) and talc (tlc). (D and E) Foliated cataclasite (sample no.: 10122102) in which serpentinite clasts exhibiting interpenetrating texture of antigorite (Atg) (D) and mesh (hourglass) texture (E) are contained in a matrix of fine-grained, randomly-oriented talc, along with minor dolomite (Dol). Cr: mesh core, Rm: mesh rim. (F) Tremolite schist (sample no.: 10122101) consisting of tremolite (Tr) and minor chlorite (Chl) overgrowing the previous metamorphic foliation. (G) Talc schist (sample no.: G02) showing a shape-preferred orientation of fine-grained talc. (H) Close up of aligned talc blades in (G).

tense fluid–rock interaction took place in connection with faulting. The serpentinite along the faults represents a foliated cataclastic zone that records brittle deformation (Fig. 3B), consisting of angular fragments that are suspended in a fine-grained, randomly-oriented talc matrix (Fig. 4D, E). These serpentinite fragments are fully serpentinized, represented by mesh (hourglass) texture and bastite of chrysotile or a mixture of lizardite (or chrysotile) and antigorite and interpenetrating texture of antigorite as well as foliated chrysotile (Fig. 4D, E). This indicates that the metasomatic growth of talc occurred simultaneously with or after the exhumation-related, chrysotile-bearing deformation (Hirauchi and Yamaguchi, 2007).

Interestingly, the argillite matrix at Jade Cove is totally metasomatized, characterized by the overgrowth of tremolite and minor chlorite along the previous metamorphic foliation (Fig. 4F). Within the mélange near the lithological boundary, varied-sized serpentinite blocks, which are now almost completely altered by the formation of talc, are incorporated as lenticular blocks (Fig. 3C), indicating that the pre-existing serpentinite was boudinaged as a competent layer within a relatively incompetent argillite-rich matrix. Talc-rich schists up to 2 m thick with folding are intercalated within the mélange (Figs. 2 and 3D). Since the talc-rich schist retains magnetite and altered spinels surrounded by chlorite coronas (Fig. 4G), it could have formed by Si-metasomatism of the pre-

Table 1
Summary of all tests performed in this study.

Run no.	Sample	Temperature (°C)	Pore fluid pressure (MPa)	Effective normal stress (MPa)	Sliding velocity (μm/s)	Friction coefficient (μ)	Initial gouge thickness (mm)	Total displacement (mm)
KH-20	tremolite schist	150	40, 80, 120	60, 120, 180	0.3, 1, 3, 10, 30, 100	0.36, 0.41, 0.46	1.12	49.9
KH-22	talc schist	20	40, 80, 120	60, 120, 180	0.3, 1, 3, 10, 30, 100	0.21, 0.21, 0.23	1.27	54.3
KH-23	argillite	20	40, 80, 120	60, 120, 180	0.3, 1, 3, 10, 30, 100	0.43, 0.43, 0.46	1.35	54.4
KH-24	serpentinite	20	40, 80, 120	60, 120, 180	0.3, 1, 3, 10, 30, 100	0.54, 0.55, 0.55	1.46	54.5
KH-25	foliated cataclasite	20	40, 80, 120	60, 120, 180	0.3, 1, 3, 10, 30, 100	0.21, 0.21, 0.27	1.32	55.1
KH-26	tremolite schist	20	40, 80, 120	60, 120, 180	0.3, 1, 3, 10, 30, 100	0.35, 0.39, 0.45	1.14	56.9
KH-28	argillite	150	40, 80, 120	60, 120, 180	0.3, 1, 3, 10, 30, 100	0.45, 0.53, 0.58	1.15	54.2
KH-29	serpentinite	150	40, 80	60, 120	0.3, 1, 3, 10, 30, 100	0.54, 0.56	1.28	22.4
KH-30	talc schist	150	40, 80, 120	60, 120, 180	0.3, 1, 3, 10, 30, 100	0.17, 0.19, 0.21	1.27	54.7
KH-31	foliated cataclasite	150	40, 80, 120	60, 120, 180	0.3, 1, 3, 10, 30, 100	0.30, 0.31, 0.33	1.35	55.9
KH-32	serpentinite	150	40, 80, 120	60, 120, 180	0.3, 1, 3, 10, 30, 100	0.60, 0.56, 0.51	1.34	54.7
KH-33	serpentinite	300	40, 80, 120	60, 120, 180	0.3, 1, 3, 10, 30, 100	0.55, 0.59, 0.55	1.38	53.8
KH-34	argillite	300	40, 80, 120	60, 120, 180	0.3, 1, 3, 10, 30, 100	0.52, 0.61, 0.68	1.36	53.6
KH-35	tremolite schist	300	40, 80, 120	60, 120, 180	0.3, 1, 3, 10, 30, 100	0.40, 0.47, 0.53	1.29	53.4
KH-36	talc schist	300	40, 80, 120	60, 120, 180	0.3, 1, 3, 10, 30, 100	0.13, 0.14, 0.16	1.36	53.8
KH-38	talc schist	150	40, 80, 120	60, 120, 180	0.3, 1, 3, 10, 30, 100	0.13, 0.16, 0.19	1.28	54.0
KH-40	foliated cataclasite	300	40, 80, 120	60, 120, 180	0.3, 1, 3, 10, 30, 100	0.32, 0.30, 0.27	1.34	53.2
KH-41	tremolite schist	400	40, 80, 120	60, 120, 180	0.3, 1, 3, 10, 30, 100	0.51, 0.53, 0.59	1.44	53.3
KH-42	argillite	400	40, 80, 120	60, 120, 180	0.3, 1, 3, 10, 30, 100	0.51, 0.59, 0.63	1.32	53.1
KH-43	tremolite schist	150	40, 80, 120	60, 120, 180	0.3, 1, 3, 10, 30, 100	0.36, 0.39, 0.43	1.25	53.3

existing serpentinite (Hirauchi et al., 2008). The talc-rich schist is characterized by a shape- and crystal-preferred orientation of fine-grained talc (Fig. 4G, H; Nagaya et al., submitted for publication). The strike and dip of foliated cataclasite and talc and tremolite schists are concordant with those of the boundary faults in the study area (Fig. 2).

3. Experimental methods

3.1. Starting materials

The starting materials used in this study were natural samples as described in Section 2, and collected from Sand Dollar Beach and Jade Cove. The samples, which include argillite (sample no.: 11121002), tremolite schist (sample no.: 10122101), serpentinite (sample no.: 10122109), talc schist (sample no.: G02) and foliated cataclasite (sample no.: 10122102), were pulverized and sieved to a grain size of < 106 μm to produce a synthetic fault gouge. All sample localities are shown in Fig. 1B. We note again that talc and tremolite schists are metasomatic products derived from serpentinite and argillite, respectively, while foliated cataclasite represents a shear zone developed along the lithological boundary. Veins and surface coatings were removed as much as possible from the samples prior to pulverization. Representative X-ray diffraction (XRD) patterns are presented in Figs. S1 and S2. A quantitative analysis using the RockJock program (Eberl, 2003) indicates that 25 wt.% of quartz is present in the argillite sample.

For the serpentinite and foliated cataclasite samples, serpentine minerals were identified using a confocal Raman microscope (alpha 300R; WITec GmbH, Ulm, Germany) at Shizuoka University, Japan. A 100× objective lens was used to focus a 488 nm solid-state laser into a 1 μm spot size. Spectra were acquired over 10–100 s of measurement time with the laser power of 6 mW. The spectrum resolution was 4 cm^{-1}. See Supplementary material for description of Raman spectra of serpentine minerals. In addition, the modal abundances of minerals and serpentine textures were determined by point counting on 28 × 48 mm thin sections (Table S1). As each textural type consists of a distinct serpentine mineral, we can roughly estimate the dominant serpentine minerals within the two samples.

3.2. Experimental procedure

We performed a series of frictional sliding experiments at pore fluid pressures (P_{fluid}) of 40–120 MPa, effective normal stresses (σ_n^{eff}) of 60–180 MPa, temperatures (T) of 20–400 °C, and sliding velocities (V) of 0.3–100 μm/s. The σ_n–T range covers shallower parts of the thrust fault (<15 km depth) in warm and cold subduction zones, when assuming $\lambda = 0.6$. The hydrothermal ring shear machine, described in detail by Niemeijer et al. (2008), was used in our frictional sliding experiments (Fig. S4A, B). In this machine, an annular sample with an initial thickness of ∼1.1–1.4 mm is located between two opposing René 41 Superalloy pistons (Fig. S4C, D). The sample is kept in place by inner and outer René 41 Superalloy confining rings, with inner and outer radii of 11 and 14 mm, respectively. To prevent slip on the piston–sample interface, a cross-hatched pattern (∼200 μm deep) is engraved on the piston faces. To reduce wall friction, the confining rings were coated with a graphite powder suspension and dried at 50 °C for 10–20 min to remove volatiles (alcohol) in the suspension, before assembly.

The piston–sample assembly was attached to the pressure-compensated piston plus the upper sealing head, was then lowered into an internally heated, water-filled pressure vessel, which in turn was sealed and placed into the Instron 1362 loading frame. The vessel was then moved upwards using the Instron ram, and the pressure-compensated piston was engaged with the upper forcing block plus the torque and axial force gauges.

An effective normal stress of 60 MPa was first applied using the Instron ram, then the furnace was switched on, heating to the desired temperature and applying a fluid pressure of 40 MPa. The system was subsequently left to equilibrate for ∼1 h. After equilibration of the entire experimental set-up, the rotary drive was switched on to give a sliding velocity of 10 μm/s until a displacement of typically ∼5 mm was reached, after which the sliding velocity was systematically stepped to 1, 0.3, 3, 30, 100 and 10 μm/s, respectively. During each experiment, pore fluid pressure and effective normal stress were simultaneously stepped in the sequence $P_{fluid} = 40$, 80, and 120 MPa and $\sigma_n^{eff} = 60$, 120, and 180 MPa, respectively. Note that the same velocity steps were applied to the second and third normal-stress sequences.

Each experiment was terminated by switching off the rotary drive and then the furnace, which resulted in a rapid decrease in the fluid pressure. The system cooled to room temperature within 20 min, after which the axial load was removed. The piston–sample assembly was then extracted and dried in an oven at 50 °C for at least 24 h. Details of the experimental conditions and key mechanical data are provided in Table 1.

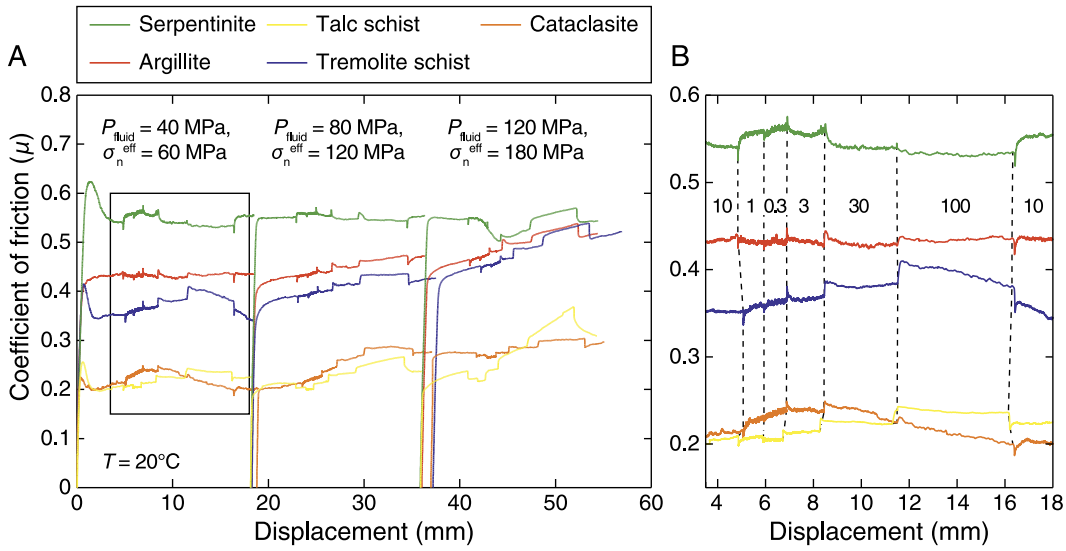

Fig. 5. (A) Coefficient of friction (μ) as a function of shear displacement sheared at pore fluid pressures (P_{fluid}) of 40, 80 and 120 MPa, effective normal stresses (σ_n^{eff}) of 60, 120 and 180 MPa, and a temperature (T) of 20 °C. (B) Enlargement of the area shown in (A) (black rectangle), showing the details of velocity steps in the first normal-stress sequence. Numbers adjacent to curves correspond to sliding velocity (μm/s). Note that the same velocity steps were applied to the second and third normal-stress sequences.

3.3. Data acquisition and processing

Shear displacement (resolution ±1 μm), axial displacement (±0.05 μm), torque (±6 Nm), and normal force (±0.05 kN) were measured externally, and the corresponding signals were recorded at a sampling rate of 10 Hz, using a 16 bit A/D converter. Torque and normal force data were corrected for seal friction to obtain the shear stress (τ) and effective normal stress (σ_n^{eff}) acting on the sample. The apparent coefficient of friction (μ) was calculated as $\mu = \tau/\sigma_n^{\text{eff}}$ and assuming no cohesion. Additional information on the details of data acquisition can be found in den Hartog et al. (2012a, 2012b).

The velocity dependence of friction was quantified in the framework of the rate and state friction model as:

$$(a-b) = \frac{\Delta\mu_{ss}}{\Delta \ln(V)} \quad (1)$$

(e.g., Ruina, 1983). Here, μ_{ss} is the steady state friction coefficient and V is the sliding velocity. Positive (a–b) values indicate an increase in friction coefficient with increasing velocity, i.e., velocity-strengthening slip behavior, which is inherently stable. Negative (a–b) values mean that the behavior is velocity-weakening, which is potentially unstable. Values of (a–b) were calculated using Eq. (1), after detrending the μ versus displacement curves for slip hardening or softening, following Blanpied et al. (1995) and den Hartog et al. (2012a). Details of the friction rate parameter ($a-b$) are shown in Tables S2 and S3.

4. Experimental results

4.1. Frictional strength

The evolution of the apparent coefficient of friction (μ) with shear displacement is shown in Figs. 5 and S5, for all temperatures. In the first normal-stress sequence, all samples, except for argillite, showed an initial peak μ at ∼0.3–1.7 mm displacement, followed by a drop in μ of up to ∼0.1, after which steady-state sliding or strain hardening was observed until the velocity steps were superimposed. The argillite sample showed strain hardening after apparent yielding at ∼0.4 mm displacement.

The steady-state apparent coefficient of friction (μ_{ss}) obtained at the first 4 mm displacement in each normal-stress sequence is plotted as a function of effective normal stress in Fig. 6A, for a temperature of 150 °C. The μ_{ss} values for the serpentinite sample slightly decreased from 0.54–0.60 at $\sigma_n^{\text{eff}} = 60$ MPa to 0.51 at $\sigma_n^{\text{eff}} = 180$ MPa, while those for the talc schist sample increased from 0.13–0.17 at $\sigma_n^{\text{eff}} = 60$ MPa to 0.19–0.21 at $\sigma_n^{\text{eff}} = 180$ MPa. The μ_{ss} of the foliated cataclasite sample ranged from 0.30 to 0.33. The μ_{ss} values for the argillite and tremolite schist samples increased from 0.45 and 0.36 at $\sigma_n^{\text{eff}} = 60$ MPa to 0.58 and 0.43–0.46 at $\sigma_n^{\text{eff}} = 180$ MPa, respectively. We also confirmed that the steady-state shear stress at all temperatures increased linearly with increasing σ_n^{eff}, indicating that a frictional regime was achieved in our experiments (Figs. S6 and S7).

The μ_{ss} obtained at the first 4 mm displacement in the second normal-stress sequence ($P_{\text{fluid}} = 80$ MPa and $\sigma_n^{\text{eff}} = 120$ MPa) is plotted against temperature in Fig. 6B. The μ_{ss} of the serpentinite sample ranged from 0.55 to 0.59. The μ_{ss} values for the talc schist sample decreased from 0.21 at $T = 20$ °C to 0.14 at $T = 300$ °C. The μ_{ss} value for the foliated cataclasite sample was 0.21 at $T = 20$ °C, increasing to 0.30–0.31 at $T = 150$–300 °C. The μ_{ss} of the argillite and tremolite schist samples increased from 0.43 and 0.39 at $T = 20$ °C to 0.59 and 0.53 at $T = 400$ °C, respectively.

4.2. Velocity dependence of friction

Values of ($a-b$) obtained at an effective normal stress of 120 MPa are plotted as a function of sliding velocity in Figs. 7 and 8, for all temperatures. The ($a-b$) values of the serpentinite sample at a given temperature were roughly independent of sliding velocity, with the values being lower at 20 °C ($a-b = -0.004$– -0.002) and higher at 150 °C ($a-b = 0.011$ – -0.018) (Fig. 7A). The ($a-b$) values of the foliated cataclasite sample slightly increased with increasing sliding velocity, ranging from −0.001–0.010 at the 1–0.3 μm/s velocity step to 0.011–0.017 at the 30–100 μm/s velocity step (Fig. 7B). The talc schist sample exhibited a narrow range in ($a-b$) at a given sliding velocity, increasing from 0.001–0.005 at the 1–0.3 μm/s velocity step to 0.009–0.017 at the 30–100 μm/s velocity step (Fig. 7C). For the argillite sample, the ($a-b$) values ranged from −0.008 to 0.007 (Fig. 8A). At a given sliding velocity, the argillite sample showed an overall decrease in ($a-b$) with increasing temperature ($T = 150$–400 °C) (Fig. 8A). Note that unstable, oscillatory (stick-slip) events were occasionally observed at $T = 400$ °C. The ($a-b$) values of the tremolite schist sample were

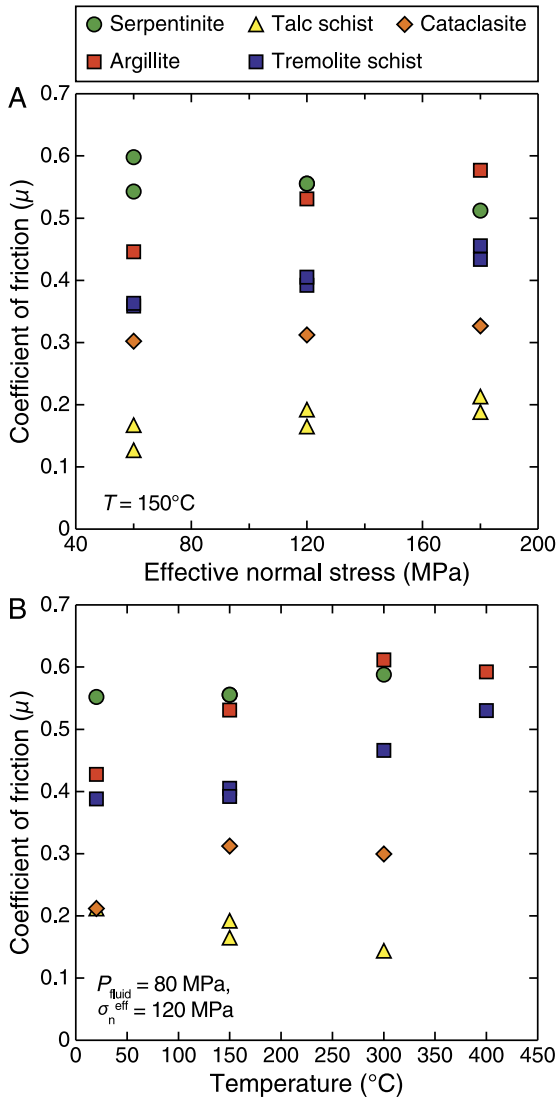

Fig. 6. Summary of friction data. All plotted measurements were taken at 4 mm shear displacement in each normal-stress sequence. (A) Coefficient of friction (μ) versus effective normal stress at a temperature (T) of 150 °C. (B) Coefficient of friction (μ) versus temperature at a pore fluid pressure (P_{fluid}) of 80 MPa and an effective normal stress (σ_n^{eff}) of 120 MPa.

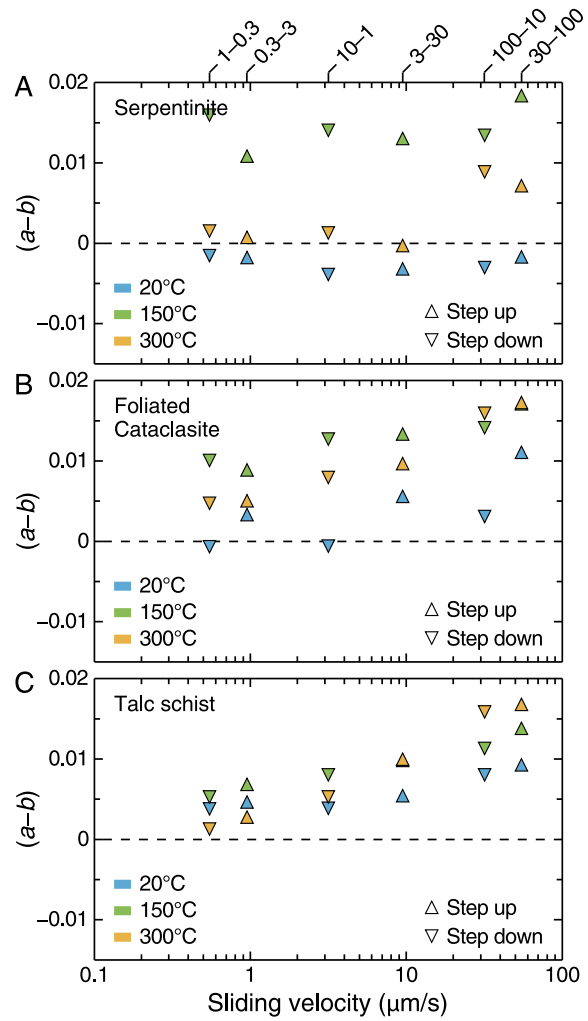

Fig. 7. Plots of the friction rate parameter ($a-b$) as a function of sliding velocity for serpentinite (A), foliated cataclasite (B) and talc schist (C) sheared at temperatures of 20, 150 and 300 °C and an effective normal stress (σ_n^{eff}) of 120 MPa.

independent of sliding velocity, with the clear exception of the 100–10 μm/s and 30–100 μm/s velocity steps, where they gradually decreased from 0.008–0.011 at $T = 150$ °C to −0.002–0.006 at $T = 400$ °C (Fig. 8B).

5. Discussion

5.1. Comparison of frictional properties between metasomatic and non-metasomatic rocks

Hydrothermal frictional sliding experiments on gouge mixtures of antigorite and quartz ($T = 300$–500 °C) for <6 days have demonstrated that metasomatic alteration of antigorite to form talc leads to significant strain weakening (Hirauchi et al., 2013). Moore and Lockner (2013), who conducted triaxial experiments on lizardite and antigorite gouges sheared between forcing blocks of granite and quartzite under hydrothermal conditions ($T = 200$–350 °C), also observed that for short (≤6 days) and long (>10 days) duration runs, a solution-transfer process causes the precipitation of serpentine and Mg-rich smectite clays (e.g., saponite) or talc, respectively, resulting in lower μ and higher ($a-b$).

Our experiments showed a marked contrast in frictional strength and slip stability between metasomatic (i.e., talc and tremolite schists) and non-metasomatic (i.e., serpentinite and argillite) rocks. Overall, metasomatic alteration of the serpentinite and argillite reduces friction and stabilizes slip, consistent with previous studies (Hirauchi et al., 2013; Moore and Lockner, 2013). The serpentinite and argillite were frictionally strong ($\mu = 0.4$–0.7) across all experimental conditions tested (Table 1; Fig. 6). Raman spectroscopic analysis reveals that antigorite is contained in the serpentinite (Fig. S3), explaining why the μ_{ss} of the serpentinite (0.5–0.6) is higher than that of other pseudomorphic, lizardite/chrysotile serpentinites (0.3–0.5) at similar conditions (e.g., Moore et al., 1997; Tesei et al., 2018). The argillite has a strong positive dependence of μ on both effective normal stress and temperature (Fig. 6); at higher effective normal stress and temperature (e.g., $\sigma_n^{\text{eff}} = 180$ MPa and $T = 150$ °C; Fig. 6), the argillite is frictionally stronger than the serpentinite. Similar trends have been observed for pure phyllosilicates such as biotite, chrysotile, and montmorillonite (Moore et al., 2004; Lu and He, 2014; Mizutani et al., 2017), illite/quartz and muscovite/quartz mixtures (i.e., argillitic lithologies) (den Hartog et al., 2012a, 2013), and phyllosilicate-bearing natural fault gouges (Boulton et al., 2014; Niemeijer et al., 2016). Moore et al. (2016) also reported that for water-saturated gouges derived from the Franciscan metasedimentary rocks, the μ_{ss} at shear displacement

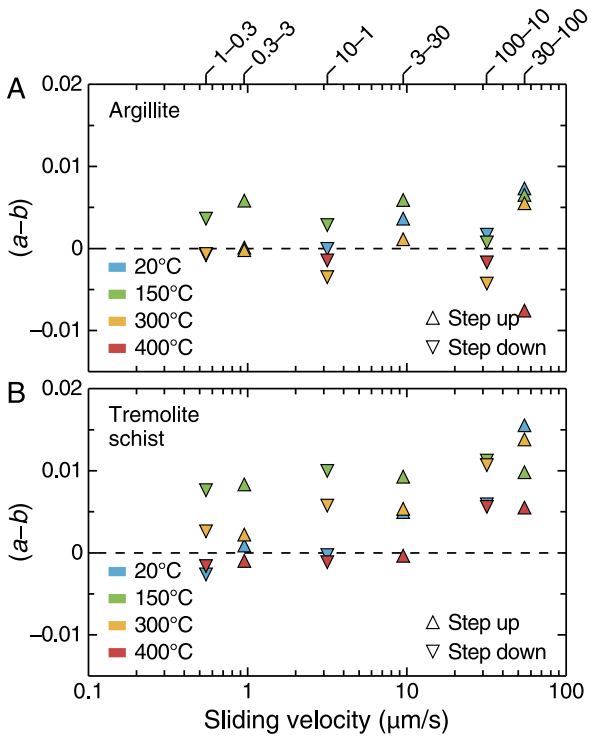

Fig. 8. Plots of the friction rate parameter $(a-b)$ as a function of sliding velocity for argillite (A) and tremolite schist (B) sheared at temperatures of 20, 150, 300 and 400 °C and an effective normal stress ($\sigma_n{}^{eff}$) of 120 MPa.

of < 5 mm gradually increased from 0.47 to 0.52 with increasing temperature ($T = 25$–250 °C and $V = 1$ μm/s). The strength of phyllosilicates is a function of the number of water molecules absorbed on the (001) planes, which act as a lubricant to reduce friction (Moore and Lockner, 2004). The observed increase in μ_{ss} with effective normal stress and temperature might be attributed to gradual loss of the water molecules by compaction and heating, respectively (e.g., Moore et al., 2004; Behnsen and Faulkner, 2012). First-principles electronic calculations based on density functional theory also imply that the roughness of potential energy surfaces contributes to macroscopic friction of phyllosilicate (Sakuma et al., 2018).

In metasomatic rocks, the talc schist exhibited very low friction (μ as low as 0.13) at our experimental conditions (Table 1), consistent with previous experimental studies that demonstrate the mechanical weakness of talc-rich rocks (Moore and Lockner, 2008; Escartín et al., 2008a; Collettini et al., 2009a; Hirauchi et al., 2013, 2016; Moore and Lockner, 2011; Niemeijer and Collettini, 2014). The decreasing trend of frictional strength with increasing temperature (Fig. 6) is similar to that observed for pure talc gouge sheared at similar conditions (Moore and Lockner, 2008). We suggest that the difference in μ between the talc schist and foliated cataclasite (Fig. 6) is attributed to the ratio of serpentine content to talc content (Fig. S1), consistent with previous friction experiments on various mixtures of serpentine and talc (Moore and Lockner, 2011). We note that the presence of 20 vol.% foliated chrysotile (Table S1) also contributes to the frictional weakness of the foliated cataclasite. Similar to the argillite, the tremolite schist also shows a positive dependence of μ on effective normal stress and temperature (Fig. 6); however, at any given experimental condition, the tremolite schist is always frictionally weaker than the argillite, with one exception at $\sigma_n{}^{eff} = 60$ MPa and $T = 400$ °C (Table 1). The observed μ values are intermediate of those obtained by Niemeijer and Collettini (2014) for their tremolite-bearing (42–46 wt.%) samples. This can be explained by the presence of 22 wt.% talc in their weaker sample and 43 wt.% calcite in their stronger sample, while our sample is a mixture of chlorite and tremolite. In addition, our tremolite schist sample has μ values intermediate between those of pure chlorite and tremolite samples sheared at $T = 290$ °C and $\sigma_n{}^{eff} = 140$ MPa (Swiatlowski et al., 2017).

Our velocity-step tests demonstrated that the serpentinite gouge exhibits velocity-weakening behavior under certain conditions (Fig. 7A), which is consistent with complex velocity-dependent frictional behavior of lizardite or chrysotile gouge sheared at 25–194 °C (Reinen et al., 1994; Moore et al., 1997). However, our experiments on serpentine-bearing samples showed that with increasing talc content (serpentinite, foliated cataclasite and talc schist in order; Fig. S1), the $(a-b)$ values become positive at all experimental conditions tested (Fig. 7), in good agreement with previous work (Moore and Lockner, 2008, 2011). For the argillite, an increase in temperature from 150 °C to 400 °C resulted in a transition from velocity strengthening to velocity weakening behavior (Fig. 8A), with stick-slip events at 400 °C. A similar transition to velocity weakening at elevated temperatures has been observed for illite/quartz and muscovite/quartz gouges sheared at $\sigma_n{}^{eff} = 170$ MPa (den Hartog et al., 2012a, 2013) as well as the Franciscan metasedimentary rock sample at $\sigma_n{}^{eff} = 100$ MPa (Moore et al., 2016). This change in velocity-dependence with increasing temperature can be interpreted in the framework of the series of microphysical models for the steady-state and transient frictional behavior of gouges in which thermally activated compaction is possible (Niemeijer and Spiers, 2007; den Hartog and Spiers, 2014; Chen and Spiers, 2016). In the microphysical model, velocity weakening is only attained when dilation due to frictional slip on grain contacts is balanced by compaction through time-dependent thermally activated process (pressure solution) of the soluble phases (e.g. quartz). A similar trend with $(a-b)$ decreasing with temperature was observed for the tremolite schist (Fig. 8B), while the transition temperature appears to be higher for the tremolite schist than for the argillite. Niemeijer and Collettini (2014) have shown that for tremolite-rich (up to 46 wt.%) fault rocks obtained from the Zuccale fault, values of $(a-b)$ change from positive to negative with increasing temperature (25–300 °C). Swiatlowski et al. (2017) have demonstrated that at a temperature of 290 °C, pure chlorite and tremolite samples are velocity strengthening and velocity weakening, respectively. This indicates that $(a-b)$ values for tremolite-rich rocks vary depending on the chlorite content, which would be a function of Al content in the fluids.

5.2. Evolution of frictional behavior via metasomatism along subduction zone faults

As mentioned above, the serpentinite body examined in this study represents abyssal peridotites derived from transform faults/fracture zones or oceanic core complexes developed in the setting of a slow- to ultraslow-spreading ridge (Hirauchi et al., 2008). The peridotites experienced subduction-related high-temperature metamorphism within the stability field of antigorite, and then were exhumed into an argillite-matrix mélange of the Franciscan Complex. On the basis of field and experimental data, we show in Fig. 9 a schematic illustration for the lithological and mechanical evolution (Stage I–III) of the serpentinite–argillite contact zone.

During Stage I, the serpentinite body was emplaced as tectonic slices within the Franciscan tectonic mélange (Hirauchi and Yamaguchi, 2007). Along the lithological boundary, the serpentinite was fragmented and incorporated as competent lenses into an incompetent argillitic matrix (Fig. 3C). This observation indicates that the serpentinite was mechanically stronger than the argillite at conditions of the upper part of the seismogenic zone, which is supported by μ values of the two samples sheared at lower ef-

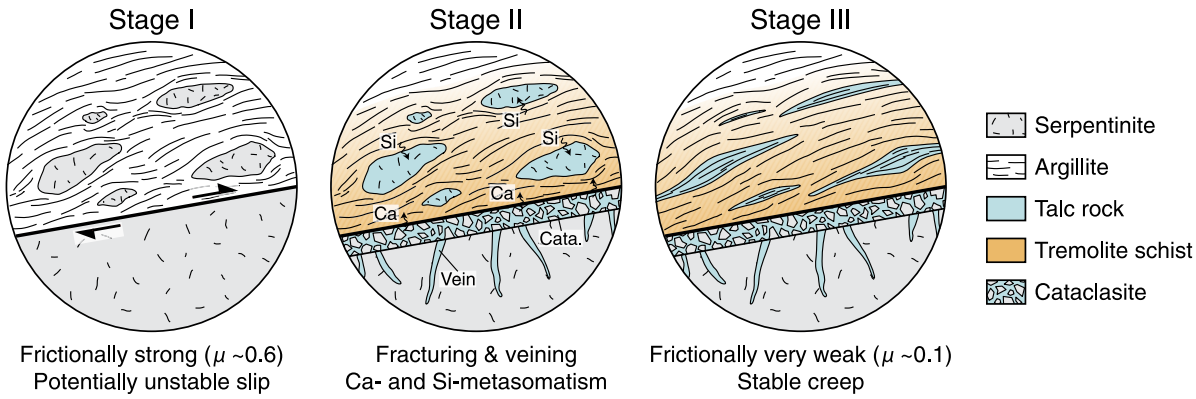

Fig. 9. Schematic diagram showing metasomatic alteration of a contact zone between argillite and serpentinite in the Franciscan Complex. Cata.: cataclasite. See the text for more details.

fective normal stresses (Fig. 6A). The observed trends in $(a - b)$ as a function of temperature (Figs. 7A and 8A) also suggest that the lithological boundary acted as intrinsically strong patches (asperities) at seismogenic depths, representing preferential sites for hosting earthquake nucleation.

Stage II is characterized by an episode of intense fluid–rock interaction along the lithological boundary (Figs. 2 and 3A, B). Since the intensity of veining associated with brittle deformation increases towards the argillite–serpentinite contact, we suggest that the lithological boundary provided an essential fluid pathway at this stage. The fluid–rock interaction involved the hydration of relict olivine and pyroxenes within the phacoids to form serpentine. After complete serpentinization, the presence of silica-rich fluids may result in the replacement of serpentine by talc (i.e., Si-metasomatism), according to the following reaction (Manning, 1997):

$$\text{serpentine} + 2SiO_2(aq) = \text{talc} + H_2O.$$

We postulate that the dissolution of quartz grains contained in the argillite (Fig. 4B) supplies significant amounts of silica into the serpentinite. The presence of hydrofractures infilled with talc within foliated cataclasites (Figs. 3B and 4D, E) suggests the attainment of fluid overpressures during fault activity. We also suggest that the serpentinite blocks within the argillite were metasomatized to talc-rich assemblages at this stage. As the tremolite schist occurs in contact with the serpentinite, the source of calcium responsible for the formation of tremolite may be attributed to the breakdown of pyroxenes within the phacoids (i.e., Ca-metasomatism; Peacock, 1987).

During continued fault activity (Stage III), strain localization may occur in the talc-rich assemblages owing to their low friction (Fig. 6). The development of shape-preferred orientation of talc (Fig. 4G, H) suggests that frictional sliding on (001) planes is the main deformation mechanism. At this stage, the talc schist acted as an intrinsically weak, ductile shear zone (Fig. 2), which is unlikely to be a nucleation site for earthquake rupture (Figs. 6 and 7C). We also note that decomposition of organic matter dispersed in the argillite contributes to the formation of CO_2-bearing veins (i.e., dolomite).

5.3. The role of ultramafic components on the degree of interplate coupling

Geological observations of exhumed subduction complexes have revealed that at depths corresponding to the seismogenic zone, precipitation of SiO_2 and $CaCO_3$ proceeds along discrete faults (e.g., Moore et al., 2007). Because quartz and calcite exhibit velocity-weakening behavior at temperatures above 100–150 °C (Chester and Higgs, 1992; Verberne et al., 2013), fluid–rock interaction in accretionary prisms will generally promote slip instability and earthquake nucleation. In contrast, in the case that the serpentinite body is in contact with argillaceous sediments, Si- and Ca-metasomatism along the serpentinite–argillite contact will lead to the development of a complex fault zone due to spatial variations in metasomatic alteration (Fig. 2) as well as due to the temperature dependence of frictional properties of all the rock units (Figs. 6–8). However, we stress that the weak, talc-rich ductile shear zones, which remain velocity strengthening even at high temperature, represent stable sliding patches on subduction thrust faults.

Along oceanic ridges spreading at < 8 cm/yr, numerous long-lived detachment faults exhume lower crustal and upper mantle rocks on the seafloor, forming oceanic core complexes (e.g., Smith et al., 2012). For instance, about half of the northern Mid-Atlantic Ridge axis is experiencing spreading by detachment faulting, implying that up to ∼25% of the seafloor is composed of oceanic core complexes (Escartín et al., 2008b). The tectonic unroofing leads to extensive serpentinization of the mantle rocks, characterized by pseudomorphic replacement of olivine and pyroxenes by lizardite and/or chrysotile (e.g., Rouméjon et al., 2015). Our experimental results indicate that if the oceanic mantle rocks start to subduct at the trench, they exhibit distinctly different frictional behavior compared to subducting sediments and oceanic crust. In particular, our results suggest the possibility that continuous subduction of the hydrated mantle rocks results in a transition from velocity weakening to velocity strengthening behavior via Si-metasomatism in a plate boundary shear zone. The onset of Si-metasomatism is primarily associated with that of quartz dissolution in underthrusting sediments at a temperature of ∼ 150 °C (Moore et al., 2007).

A number of serpentinite mud volcanoes exist in the Izu-Bonin-Mariana (IBM) forearc region, implying the existence of an extensively serpentinized mantle wedge of the Philippine Sea (PHS) plate (e.g., Fryer, 2012). In the Kanto district of central Japan, north of the IBM forearc, the PHS plate is subducting northwestward beneath the continental plate, and the Pacific (PAC) plate is subducting westward beneath the PHS and continental plates. Based on seismic tomographic data beneath Kanto, Nakajima et al. (2009) found that the wedge-shaped serpentinized mantle in the PHS plate is subducting down to depths of ∼80 km due to the low geothermal gradient. Furthermore, Uchida et al. (2009) revealed that on the upper surface of the PAC plate, the plate interface overlain by the serpentinized mantle of the PHS plate is characterized by weak interplate coupling and low seismic activity. Since the dominant serpentine phases present in the serpentinite muds sampled are lizardite and chrysotile (Fryer, 2012), which become velocity weakening particularly at elevated temperatures (Fig. 7A;

Moore et al., 1997, 2004), we suggest that metasomatic alteration of lizardite/chrysotile to form talc after subduction enables the plate boundary fault to slip aseismically, lowering the coupling. We caution, however, that the degree of interplate coupling is also influenced by fluid content and topographic reliefs on the subducting plate, which contribute to values of effective normal stress (e.g., Wang and Bilek, 2011; Scholz and Campos, 2012; Heise et al., 2017).

Although the metasomatic reaction zone observed in our study formed at shallow seismogenic depths, our results are applicable to any tectonic setting where ultramafic and crustal rocks are juxtaposed. For instance, Si-rich fluids liberated from the subducting oceanic slab migrate into the overlying forearc mantle wedge, inducing serpentinization and subsequent metasomatic alteration (Manning, 1997; Bebout and Penniston-Dorland, 2016). Seismic tomographic studies indicate that in the warm Nankai subduction zone, the shallow ($<$ 60 km depth) mantle wedge is partially serpentinized (e.g., Hirose et al., 2008). The weak interplate coupling along the slab–mantle interfaces (e.g., Yoshioka and Matsuoka, 2013) can be explained by ductile deformation of talc-rich shear zones formed via Si-metasomatism, in addition to stable frictional sliding of antigorite, a high-temperature serpentine phase, which tends to exhibit velocity strengthening behavior in its stability field (Moore et al., 1997; Takahashi et al., 2011). Indeed, geological studies of exhumed subduction complexes at greenschist to eclogite facies conditions have reported the occurrence of talc- or tremolite-bearing metasomatic reaction zones between mantle wedge-derived antigorite serpentinite and pelitic schist (Aoya et al., 2013). On the other hand, in the cold Tohoku subduction zone, the degree of interplate coupling is found to be spatially heterogeneous on the slab–mantle interface (Suwa et al., 2006). Yamamoto et al. (2008) shows a close correlation between areas of high V_p/V_s ratios within the shallow ($<$ 60 km) mantle wedge and weak interplate coupling, suggesting that low-temperature serpentinization and subsequent metasomatic alteration allow the plate interface to slip stably.

6. Conclusions

Metasomatic alteration at the ultramafic–sedimentary contact leads to the formation of a reaction zone consisting of hydrous minerals. To investigate the evolution of frictional strength and slip stability via Ca- and Si-metasomatism, we performed a series of hydrothermal frictional sliding experiments on simulated gouge prepared from the metasomatic (talc and tremolite schists) and non-metasomatic (serpentinite and argillite) rocks in the Franciscan accretionary complex. On the basis of our mechanical data, we can conclude the following:

1. Pseudomorphic serpentinite as tested in this study is frictionally strong, with the coefficient of friction (μ) ranging from 0.5 to 0.6.
2. Talc schist has a very low μ (as low as 0.1), with a negative dependence of μ on temperature.
3. Argillite and tremolite schist exhibit an increase in μ with increasing effective normal stress and temperature, up to 0.7 and 0.6, respectively. The former is frictionally stronger than the latter at a given experimental condition.
4. With increasing talc content, serpentine-bearing rock becomes more velocity strengthening. Talc schist has a positive dependence of $(a - b)$ on sliding velocity.
5. For argillite and tremolite schist, friction transitions from velocity strengthening to velocity weakening with increasing temperature. The temperature transitioning to velocity weakening is lower for the former than for the latter.
6. The metasomatic growth of talc in ultramafic systems plays a role in reducing friction, stabilizing slip, and preventing earthquake propagation along the fault.

Declaration of competing interest

The authors declare that they have no known competing financial interests or personal relationships that could have appeared to influence the work reported in this paper.

Acknowledgements

We appreciate the advice of Christopher Spiers and Colin Peach when using the Utrecht ring shear machine. We greatly appreciate constructive comments by Diane Moore and Telemaco Tesei. Raman spectroscopic and XRD analyses were carried out with the help of Tatsuhiko Kawamoto and Keishi Okazaki, respectively. We would also like to thank Jun Kameda for his help in conducting XRD-RockJock analyses. Technical support in maintaining the ring shear machine was provided by Thony van der Gon Netscher, Gert Kastelein and Eimert de Graaff. This study was funded by a Grant-in-Aid for Scientific Research on Innovative Areas (No. 26109005) and the Ministry of Education, Culture, Sports, Science and Technology (MEXT) of Japan, under its Earthquake and Volcano Hazards Observation and Research Program.

Appendix A. Supplementary material

Supplementary material related to this article can be found online at https://doi.org/10.1016/j.epsl.2019.115967.

References

Aoya, M., Endo, S., Mizukami, T., Wallis, S.R., 2013. Paleo-mantle wedge preserved in the Sambagawa high-pressure metamorphic belt and the thickness of forearc continental crust. Geology 41, 451–454.

Bebout, G.E., Barton, M.D., 2002. Tectonic and metasomatic mixing in a high-T, subduction-zone mélange—insights into the geochemical evolution of the slab–mantle interface. Chem. Geol. 187, 79–106.

Bebout, G.E., Penniston-Dorland, S.C., 2016. Fluid and mass transfer at subduction interfaces—the field metamorphic record. Lithos 240–243, 228–258.

Behnsen, J., Faulkner, D.R., 2012. The effect of mineralogy and effective normal stress on frictional strength of sheet silicates. J. Struct. Geol. 42, 49–61.

Blanpied, M.L., Lockner, D.A., Byedee, J.D., 1995. Frictional slip of granite at hydrothermal conditions. J. Geophys. Res. 100, 13045–13064.

Boulton, C., Moore, D.E., Lockner, D.A., Toy, V.G., Townend, J., Sutherland, R., 2014. Frictional properties of exhumed fault gouges in DFDP-1 cores, Alpine Fault, New Zealand. Geophys. Res. Lett. 41, 356–362.

Burgette, R.J., Weldon II, R.J., Schmidt, D.A., 2009. Interseismic uplift rates for western Oregon and along-strikevariation in locking on the Cascadia subduction zone. J. Geophys. Res. 114, B01408.

Chen, J., Spiers, C.J., 2016. Rate and state frictional and healing behavior of carbonate fault gouge explained using microphysical model. J. Geophys. Res. 121, 8642–8665.

Chester, F.M., Higgs, N.G., 1992. Multimechanism friction constitutive model for ultrafine quartz gouge at hypocentral conditions. J. Geophys. Res. 97, 1859–1870.

Coleman, R.G., 2000. Prospecting for ophiolites along the California continental margin. Spec. Pap., Geol. Soc. Am. 349, 351–364.

Collettini, C., Niemeijer, A., Viti, C., Marone, C., 2009a. Fault zone fabric and fault weakness. Nature 462, 907–910.

Collettini, C., Viti, C., Smith, S.A.F., Holdsworth, R.E., 2009b. Development of interconnected talc networks and weakening of continental low-angle normal faults. Geology 37, 567–570.

den Hartog, S.A.M., Niemeijer, A.R., Spiers, C.J., 2012a. New constraints on megathrust slip stability under subduction zone P–T conditions. Earth Planet. Sci. Lett. 353–354, 240–252.

den Hartog, S.A.M., Peach, C.J., de Winter, D.A.M., Spiers, C.J., Shimamoto, T., 2012b. Frictional properties of megathrust fault gouges at low sliding velocities: new data on effects of normal stress and temperature. J. Struct. Geol. 38, 156–171.

den Hartog, S.A.M., Niemeijer, A.R., Spiers, C.J., 2013. Friction on subduction megathrust faults: beyond the illite–muscovite transition. Earth Planet. Sci. Lett. 373, 8–19.

den Hartog, S.A.M., Spiers, C.J., 2014. A microphysical model for fault gouge friction applied to subduction megathrusts. J. Geophys. Res. 119, 1510–1529.

Eberl, D.D., 2003. User's Guide to RockJock-A Program for Determining Quantitative, Mineralogy from Powder X-Ray Diffraction Data. USGS Open-File Report 03–78.

Ernst, W.G., 1980. Mineral paragenesis in Franciscan metagraywackes of the Nacimiento block, a subduction complex of the southern California Coast Ranges. J. Geophys. Res. 85, 7045–7055.

Ernst, W.G., 2011. Accretion of the Franciscan Complex attending Jurassic–Cretaceous geotectonic development of northern and central California. Geol. Soc. Am. Bull. 123, 1667–1678.

Escartín, J., Andreani, M., Hirth, G., Evans, B., 2008a. Relationships between the microstructural evolution and the rheology of talc at elevated pressures and temperatures. Earth Planet. Sci. Lett. 268, 463–475.

Escartín, J., Smith, D.K., Cann, J., Schouten, H., Langmuir, C.H., Escrig, S., 2008b. Central role of detachment faults in accretion of slow-spreading oceanic lithosphere. Nature 455, 790–794.

Evans, B.W., 2004. The serpentinite multisystem revisited: chrysotile is metastable. Int. Geol. Rev. 46, 479–506.

Fryer, P., 2012. Serpentinite mud volcanism: observations, processes, and implications. Annu. Rev. Mar. Sci. 4, 345–373.

Hall Jr., C.A., 1991. Geology of the Point Sur-Lopez Point region, Coast Ranges, California: a part of the Southern California allochthon. Spec. Pap., Geol. Soc. Am. 266.

Heise, W., Caldwell, T.G., Bannister, S., Bertrand, E.A., Ogawa, Y., Bennie, S.L., Ichihara, H., 2017. Mapping subduction interface coupling using magnetotellurics: Hikurangi margin, New Zealand. Geophys. Res. Lett. 44, 9261–9266.

Hirauchi, K., Yamaguchi, H., 2007. Unique deformation processes involving the recrystallization of chrysotile within serpentinite: implications for aseismic slip events within subduction zones. Terra Nova 19, 454–461.

Hirauchi, K., Tamura, A., Arai, S., Yamaguchi, H., Hisada, K., 2008. Fertile abyssal peridotites within the Franciscan subduction complex, central California: possible origin as detached remnants of oceanic fracture zones located close to a slow-spreading ridge. Lithos 105, 319–328.

Hirauchi, K., Katayama, I., Uehara, S., Miyahara, M., Takai, Y., 2010. Inhibition of subduction thrust earthquakes by low-temperature plastic flow in serpentine. Earth Planet. Sci. Lett. 295, 349–357.

Hirauchi, K., den Hartog, S.A.M., Spiers, C.J., 2013. Weakening of the slab–mantle wedge interface induced by metasomatic growth of talc. Geology 41, 75–78.

Hirauchi, K., Fukushima, K., Kido, M., Muto, J., Okamoto, A., 2016. Reaction-induced rheological weakening enables oceanic plate subduction. Nat. Commun. 7, 12550.

Hirose, F., Nakajima, J., Hasegawa, A., 2008. Three-dimensional seismic velocity structure and configuration of the Philippine Sea slab in southwestern Japan estimated by double-difference tomography. J. Geophys. Res. 113, B09315.

Holdsworth, R.E., van Diggelen, E.W.E., Spiers, C.J., de Bresser, J.H.P., Walker, R.J., Bowen, L., 2011. Fault rocks from the SAFOD core samples: implications for weakening at shallow depths along the San Andreas Fault, California. J. Struct. Geol. 33, 132–144.

Ikari, M.J., Niemeijer, A.R., Spiers, C.J., Kopf, A.J., Saffer, D.M., 2013. Experimental evidence linking slip instability with seafloor lithology and topography at the Costa Rica convergent margin. Geology 41, 891–894.

Jennings, C.W., 1958. Geologic map of California: San Luis Obispo sheet. California Division of Mines and Geology. Scale 1:250,000.

King, R.L., Kohn, M.J., Eiler, J.M., 2003. Constraints on the petrologic structure of the subduction zone slab-mantle interface from Franciscan Complex exotic ultramafic blocks. Geol. Soc. Am. Bull. 115, 1097–1109.

Lu, Z., He, C., 2014. Frictional behavior of simulated biotite fault gouge under hydrothermal conditions. Tectonophysics 622, 62–80.

Manning, C.E., 1997. Coupled reaction and flow in subduction zones: silica metasomatism in the mantle wedge. In: Jamtveit, B., Yardley, B.W.D. (Eds.), Fluid Flow and Transport in Rocks. Chapman and Hall, London, pp. 139–147.

Mizutani, T., Hirauchi, K., Lin, W., Sawai, M., 2017. Depth dependence of the frictional behavior of montmorillonite fault gouge: implications for seismicity along a décollement zone. Geophys. Res. Lett. 44, 5383–5390.

Moore, D.E., Lockner, D.A., 2004. Crystallographic controls on the frictional behavior of dry and water-saturated sheet structure minerals. J. Geophys. Res. 109, B03401.

Moore, D.E., Lockner, D.A., 2008. Talc friction in the temperature range 25 °C–400 °C: relevance for fault-zone weakening. Tectonophysics 449, 120–132.

Moore, D.E., Lockner, D.A., 2011. Frictional strengths of talc-serpentine and talc-quartz mixtures. J. Geophys. Res. 116, B01403.

Moore, D.E., Lockner, D.A., 2013. Chemical controls on fault behavior: weakening of serpentinite sheared against quartz-bearing rocks and its significance for fault creep in the San Andreas system. J. Geophys. Res. 118, 2558–2570.

Moore, D.E., Rymer, M.J., 2007. Talc-bearing serpentinite and the creeping section of the San Andreas Fault. Nature 448, 795–797.

Moore, D.E., Lockner, D.A., Ma, S., Summers, R., Byerlee, J.D., 1997. Strengths of serpentinite gouges at elevated temperatures. J. Geophys. Res. 102, 14787–14801.

Moore, D.E., Lockner, D.A., Tanaka, H., Iwata, K., 2004. The coefficient of friction of chrysotile gouge at seismogenic depths. Int. Geol. Rev. 46, 385–398.

Moore, D.E., Lockner, D.A., Hickman, S., 2016. Hydrothermal frictional strengths of rock and mineral samples relevant to the creeping section of the San Andreas Fault. J. Struct. Geol. 89, 153–167.

Moore, J.C., Rowe, C., Meneghini, F., 2007. How accretionary prisms elucidate seismogenesis in subduction zones. In: Dixon, T., Moore, J.C. (Eds.), The Seismogenic Zone of Subduction Thrust Faults. Columbia University Press, New York, pp. 288–315.

Nagaya, T., Okamoto, A., Oyanagi, R., Seto, Y., Miyake, A., Uno, M., Muto, J., Wallis, S.R., submitted for publication. Talc CPO determined by improved EBSD procedure for sheet silicates: implications for anisotropy at the slab–mantle interface due to Si-metasomatism. Am. Mineral.

Nakajima, J., Hirose, F., Hasegawa, A., 2009. Seismotectonics beneath the Tokyo metropolitan area, Japan: effect of slab-slab contact and overlap on seismicity. J. Geophys. Res. 114, B08309.

Niemeijer, A.R., 2018. Velocity-dependent slip weakening by the combined operation of pressure solution and foliation development. Sci. Rep. 8, 4724.

Niemeijer, A.R., Collettini, C., 2014. Frictional properties of a low-angle normal fault under in situ conditions: thermally-activated velocity weakening. Pure Appl. Geophys. 171, 2641–2664.

Niemeijer, A.R., Spiers, C.J., 2007. A microphysical model for strong velocity weakening in phyllosilicate-bearing fault gouges. J. Geophys. Res. 112, B10405.

Niemeijer, A.R., Spiers, C.J., Peach, C.J., 2008. Frictional behaviour of simulated quartz fault gouges under hydrothermal conditions: results from ultra-high strain rotary shear experiments. Tectonophysics 460, 288–303.

Niemeijer, A.R., Boulton, C., Toy, V.G., Townend, J., Sutherland, R., 2016. Large-displacement, hydrothermal frictional properties of DFDP-1 fault rocks, Alpine Fault, New Zealand: implications for deep rupture propagation. J. Geophys. Res. 121, 624–647.

Oleskevich, D.A., Hyndman, R.D., Wang, K., 1999. The updip and downdip limits to great subduction earthquakes: thermal and structural models of Cascadia, South Alaska, SW Japan, and Chile. J. Geophys. Res. 104, 14965–14991.

Peacock, S.M., 1987. Serpentinization and infiltration metasomatism in the Trinity peridotite, Klamath province, northern California: implications for subduction zones. Contrib. Mineral. Petrol. 95, 55–70.

Reinen, L.A., Weeks, J.D., Tullis, T.E., 1994. The frictional behavior of lizardite and antigorite serpentinites: experiments, constitutive models, and implications for natural faults. Pure Appl. Geophys. 143, 317–358.

Rouméjon, S., Cannat, M., Agrinier, P., Godard, M., Andreani, M., 2015. Serpentinization and fluid pathways in tectonically exhumed peridotites from the Southwest Indian Ridge (62–65 °E). J. Petrol. 56, 703–734.

Ruina, A., 1983. Slip instability and state variable friction laws. J. Geophys. Res. 88, 10359–10370.

Sakuma, H., Kawai, K., Katayama, I., Suehara, S., 2018. What is the origin of macroscopic friction? Sci. Adv. 4, eaav2268.

Scholz, C.H., Campos, J., 2012. The seismic coupling of subduction zones revisited. J. Geophys. Res. 117, B05310.

Schwartz, S., Guillot, S., Reynard, B., Lafay, R., Debret, B., Nicollet, C., Lanari, P., Auzende, A.L., 2013. Pressure–temperature estimates of the lizardite/antigorite transition in high pressure serpentinites. Lithos 178, 197–210.

Smith, D.K., Escartín, J., Schouten, H., Cann, J.R., 2012. Active long-lived faults emerging along slow-spreading mid-ocean ridges. Oceanography 25, 94–99.

Spandler, C., Hermann, J., Faure, K., Mavrogenes, J.A., Arculus, R.J., 2008. The importance of talc and chlorite "hybrid" rocks for volatile recycling through subduction zones; evidence from the high-pressure subduction mélange of New Caledonia. Contrib. Mineral. Petrol. 155, 181–198.

Suwa, Y., Miura, S., Hasegawa, A., Sato, T., Tachibana, K., 2006. Interplate coupling beneath NE Japan inferred from three-dimensional displacement field. J. Geophys. Res. 111, B04402.

Swiatlowski, J.L., Moore, D.E., Lockner, D.A., 2017. The influence of metasomatic alteration on the frictional properties of serpentinite-bearing gouge in the Bartlett Springs Fault, northern California. Geol. Soc. Am. Abstr. Programs 49 (6), 288-17.

Takahashi, M., Uehara, S.-I., Mizoguchi, K., Shimizu, I., Okazaki, K., Masuda, K., 2011. On the transient response of serpentine (antigorite) gouge to stepwise changes in slip velocity under high-temperature conditions. J. Geophys. Res. 116, B10405.

Tesei, T., Harbord, C.W.A., De Paola, N., Collettini, C., Viti, C., 2018. Friction of mineralogically controlled serpentinites and implications for fault weakness. J. Geophys. Res. 123, 6976–6991.

Trütner, S., Hüpers, A., Ikari, M.J., Yamaguchi, A., Kopf, A.J., 2015. Lithification facilitates frictional instability in argillaceous subduction zone sediments. Tectonophysics 665, 177–185.

Uchida, N., Nakajima, J., Hasegawa, A., Matsuzawa, T., 2009. What controls interplate coupling?: Evidence for abrupt change in coupling across a border between two overlying plates in the NE Japan subduction zone. Earth Planet. Sci. Lett. 283, 111–121.

Verberne, B.A., Spiers, C.J., Niemeijer, A.R., de Bresser, J.H.P., de Winter, D.A.M., Plümper, O., 2013. Frictional properties and microstructure of calcite-rich fault gouges sheared at sub-seismic sliding velocities. Pure Appl. Geophys. 171, 2617–2640.

Vrolijk, P., 1990. On the mechanical role of smectite in subduction zones. Geology 18, 703–707.

Wang, K., Bilek, S.L., 2011. Do subducting seamounts generate or stop large earthquakes? Geology 39, 819–822.

Yamamoto, Y., Hino, R., Suzuki, K., Ito, Y., Yamada, T., Shinohara, M., Kanazawa, T., Aoki, G., Tanaka, M., Uehira, K., Fujie, G., Kaneda, Y., Takanami, T., Sato, T., 2008. Spatial heterogeneity of the mantle wedge structure and interplate coupling in the NE Japan forearc region. Geophys. Res. Lett. 35, L23304.

Yoshioka, S., Matsuoka, Y., 2013. Interplate coupling along the Nankai Trough, southwest Japan, inferred from inversion analyses of GPS data: effects of subducting plate geometry and spacing of hypothetical ocean-bottom GPS stations. Tectonophysics 600, 165–174.